Ultrafast thermal modulation dynamics during ripple formation induced by a femtosecond laser multi-pulse vortex beam

Guangqing Du[1] ⓘ, Waqas Ahmad[1] ⓘ, Qing Yang[2] and Feng Chen[1],* ⓘ

[1] State Key Laboratory for Manufacturing System Engineering and Shaanxi Key Laboratory of Photonics Technology for Information, School of Electronic Science and Engineering, Xi'an Jiaotong University, Xi'an 710049, People's Republic of China
[2] School of Instrument Science and Technology, Xi'an Jiaotong University, Xi'an 710049, People's Republic of China

E-mail: chenfeng@mail.xjtu.edu.cn

CrossMark

Abstract

This work theoretically investigated the ultrafast thermal modulation dynamics during early formation of ripples on an Au film induced by femtosecond laser multi-pulse vortex beam irradiation. An extended two-temperature dynamics model that comprehensively considers optical interference modulation for the formation of seed ripples, transient reflectivity and non-equilibrium thermal transfer was self-consistently built to predict high-contrast ripple formation. The two-dimensional evolution of electron and phonon temperature modulations during ripple formation in a high non-equilibrium state of Au film were obtained via femtosecond laser multi-pulse vortex beam irradiation. It was revealed that ripple contrast can be significantly amplified by shortening the laser wavelength, increasing the pulse number, or enlarging the laser fluence of the vortex beam. Moreover, the electron–phonon coupling time during ripple formation is fully explored in detail. This study provides valuable insights into optimizing laser parameters for controlled high-contrast ripple formation on Au films.

1. Introduction

Femtosecond laser processing of materials has exhibited huge potential in manufacturing advanced functional structures due to its inherent merits of high precision, flexibility, and versatile fabrication ability. Femtosecond laser-induced periodic surface structures, called ripples, have constantly attracted much interest in achieving advanced biomimetic architectures, meta-surfaces, and friction devices [1–6]. Unfortunately, it has been experimentally observed that ripple morphology usually

deteriorates due to the emerging thermal traces decorated on the ripples [7], hindering the potential applications of such ripples.

Physically, it is generally accepted that high-quality seed ripples can be initially formed due to early electromagnetic interference between the incident laser and the scattering surface plasmon waves [8–11]. What is more, the complex thermal and fluidic dynamics can play an even more decisive role in governing the resultant ripple morphology. In particular, it has been validated that the early non-equilibrium thermal dynamics, also called two-temperature dynamics, could be responsible for possible high-quality ripple formation [12, 13]. Wang and Guo experimentally revealed that the dominant

---

* Author to whom any correspondence should be addressed.

dynamics of the electron–phonon (e–p) coupling and the hot electron diffusion in a two-temperature framework can affect the morphological clarity of ripples, with the desirable effect of giving rise to sharper ripples on metals with a larger e–p coupling factor [14]. Until now, most studies have focused on the electromagnetic mechanism and the two-temperature role in explaining the characteristics of ripples on a wide range of materials by controlling a conventional Gaussian femtosecond laser [15–19].

Recently, it has been frequently observed that a vortex beam can serve as an advanced method for achieving ripples with radial and annular stripes that cannot be easily realized by a conventional Gaussian beam [20–23]. Nivas *et al* experimentally demonstrated the flexibility of controlling surface ripple properties using an optical vortex beam [24]. Our recent theoretical work revealed unusual vortical characteristics during femtosecond laser vortex beam heating of film system targets in a non-ripple regime [25, 26]. Given the ripple formation, the vortical heating dynamics become even more sophisticated due to the synchronous multi-dynamic processes in the highly e–p decoupled state of the target. It thus becomes critically important to explore the unobserved vortical thermalization dynamics in the ripple modulation regime for a good understanding of the morphological characteristics of ripples. However, to the best of our knowledge, the early dynamics of vortex thermalization during ripple formation under femtosecond multi-pulse vortex beam irradiations in highly non-equilibrium conditions have not yet been extensively studied.

In this paper, we present a theoretical investigation of vortical thermal dynamics during the formation of annular ripples in a highly non-equilibrium state of Au film. An extended two-temperature model is proposed, which comprehensively considers the optical interference modulation for seed ripples, the transient reflectivity, and the non-equilibrium thermal transfer dynamics. We will investigate the evolution dynamics of ripples in the early stage of thermal modulation on an Au film triggered by a femtosecond laser vortex beam. Moreover, multi-parameter control for ripple contrast in the early non-equilibrium phase following vortex beam excitation will be fully explored.

2. Modelling and methods

Generally, as a femtosecond laser pulse irradiates a metal target, the electron sub-system is initially pumped to a high-temperature state in the sub-layer of the target. Then, the excited electron gas dissipates its energy into the deeper bulk of the target by electron thermal diffusion on a femtosecond-to-picosecond timescale. Meanwhile, the phonon sub-system is locally disturbed in the electron thermal diffusion region owing to the e–p coupling mechanism, typically on a picosecond timescale. The above-mentioned processes can be described by the well-known two-temperature model, which has been intensively investigated for a wide range of materials [27–30]. However, the conventional two-temperature model is insufficient for directly evaluating ripple modulation dynamics

and thus cannot accurately predict ripple formation. Here, we introduce an extended two-temperature model that especially considers the synchronous optical modulation within a femtosecond laser multi-pulse vortex beam to predict the early thermal dynamics of ripple formation. To focus on the thermal dynamics of ripple evolution, we have reasonably ignored the details of surface wave interference instead of equivalently treating the interference pattern as a periodically modulated thermal source. The periodic modulation of seed ripples is considered for the spatial energy deposition rate within the vortex beam. The period-modulated profile carried on the vortex beam is applied as the thermal source for the two-temperature equation. Therefore, this brings an essential difference to the predicted results compared with previous ones in a non-ripple regime [26], and is particularly qualified for obtaining the ripple thermal dynamics driven by an advanced vortex beam compared with the non-modulated energy absorption rate model. Thus, the laser energy absorption rate in the ripple region can be well defined by a cosine-modulated envelope on the vortex beam, as mathematically expressed by

$$
Q_{\text{ripples}} = \sqrt{\frac{4\ln 2}{\pi}} \frac{1-R}{\delta + \delta_{\text{b}}} \sum_{i=1}^{N} \cos\left(\frac{2\pi r}{P}\right) \frac{F_i}{t_{\text{p}}} \frac{4r^2}{\omega_0^2} \exp\left(-2r^2/\omega_0^2\right)
$$
$$
\times \exp\left[\left(-\frac{z}{\delta + \delta_{\text{b}}}\right) - 4\ln 2\left(\frac{t - 2t_{\text{p}} - (i-1)\Delta}{t_{\text{p}}}\right)^2\right]. \tag{1}
$$

Here, r and z denote the coordinates in the width and depth directions in an axially symmetric two-dimensional (2D) geometry of the Au film target. The topological charge for the vortex beam is set as the basic ± 1. The waist ω_0 of the fundamental Gaussian profile associated with the vortex beam is set as 4 μm. δ is the optical skin depth for Au film under laser irradiation at 800 nm wavelength is set as 15.5 nm, and δ_{b}, the electron ballistic transfer length for Au film, is typically taken as 100 nm. R is the temperature-modulated surface reflectivity in the ripple region. P indicates the period of the ripples. F_i denotes the fluence for the ith pulse of a femtosecond laser multi-pulse vortex beam. t_{p} is the full width at half maximum (FWHM) pulse duration for the respective pulses of the multi-pulse vortex beam. Δ is the pulse temporal separation in a multi-pulse sequence. N denotes the pulse number in a femtosecond laser vortex beam sequence.

In this model, we apply the dynamic complex dielectric function for Au target, which can be split into real and imaginary parts as follows [31]:

$$
\varepsilon = 1 - \frac{\omega_{\text{p}}^2}{\omega^2 + \nu_{\text{m}}^2} + i\frac{\nu_{\text{m}}}{\omega}\frac{\omega_{\text{p}}^2}{\omega^2 + \nu_{\text{m}}^2} \tag{2}
$$

where $\omega_{\text{p}}^2 = \frac{e^2 n_{\text{e}}}{\varepsilon_0 m_{\text{e}}}$ means the plasma frequency of Au. The total scattering rate of electrons is considered as the sum of rates of the separate mechanisms including electron–electron (e–e) scattering and e–p scattering, written as $\nu_{\text{m}} = 1/\tau_{\text{ee}} + 1/\tau_{\text{ep}}$, where τ_{ee} and τ_{ep} are the temperature-dependent scattering times for the e–e and e–p scattering modes. Based

on the Fresnel law, the temperature-dependent reflectivity on a ripple-modulated Au film surface can be written as follows [31]:

$$R = \frac{[\text{Re}(\sqrt{\varepsilon}) - 1]^2 + [\text{Im}(\sqrt{\varepsilon})]^2}{[\text{Re}(\sqrt{\varepsilon}) + 1]^2 + [\text{Im}(\sqrt{\varepsilon})]^2}. \tag{3}$$

The modified two-temperature model in consideration of ripple thermal modulation can be mathematically described by [32]

$$C_e \frac{\partial T_e}{\partial t} = \nabla(k_e \nabla T_e) - G(T_e - T_p) + Q_{\text{ripples}} \tag{4}$$

$$C_p \frac{\partial T_p}{\partial t} = G(T_e - T_p). \tag{5}$$

Here, T_e and T_p represent the respective temperatures for the electron and phonon systems in the ripple thermal modulation region, C_e is the thermal capacity for electrons of Au film, taken as $C_e = \gamma T$, and C_p is the thermal capacity for phonons. k_e is the temperature-dependent thermal conductivity for electrons in the highly non-equilibrium state of Au film, taken in the following form [33]:

$$k_e = \chi \frac{\left(\theta_e^2 + 0.16\right)^{5/4} \left(\theta_e^2 + 0.44\right) \theta_e}{\left(\theta_e^2 + 0.092\right)^{1/2} \left(\theta_e^2 + \eta\theta_p\right)}. \tag{6}$$

The temperature-dependent e–p coupling strength is adopted, written as [33]

$$G = g_0 \left[A_e / B_p (T_e + T_p) + 1\right] \tag{7}$$

where g_0 is the e–p coupling strength in the unexcited state at a room temperature of 300 K, and A_e and B_p are constant coefficients.

Numerically, the coupling partial differential equations (1)–(7) are solved by applying the commercial software COMSOL Multiphysics. Firstly, we build the 2D axial symmetry geometry of Au film with a surface width of 6 μm and a thickness of 1 μm and define the electron and phonon heat transfer equations within the geometric domain. Secondly, the initial and boundary conditions are reasonably set for solving the coupling partial differential equations as follows: the electron and phonon systems are initially kept at 300 K at room temperature. The heat energy loss from the Au film system to the front surface is reasonably neglected during femtosecond-to-picosecond periods, and perfect thermal insulation is assumed at the rear surface and bilateral sides of the Au film system. Thirdly, an adaptive meshing-generating program is carried out to discretize the Au target geometry. Lastly, we run the overall procedure to obtain the thermal dynamics during ripple formation by varying the crucial parameters of the femtosecond laser vortex beam, as will be discussed in detail in the next section. The relevant simulation parameters used for Au are as follows [34]: $\gamma = 68$ J m^{-3} K^{-2}, $C_p = 2.5 \times 10^6$ J m^{-3} K^{-1}, $A_e = 1.18 \times 10^7$ s^{-1} K^{-2}, $B_p = 1.25 \times 10^{11}$ s^{-1} K^{-1} and $g_0 = 0.21 \times 10^{17}$ J m^{-3} s^{-1} K^{-1}.
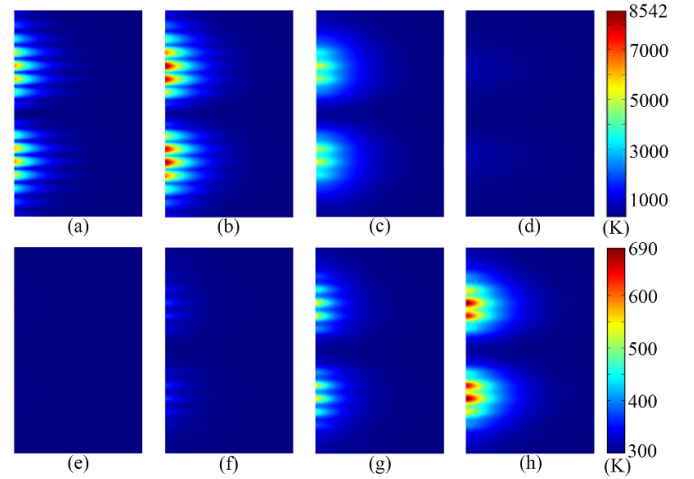

Figure 1. The 2D maps of temperature modulation in the ripple region at a sub-layer of Au film induced by a femtosecond laser two-pulse vortex beam. The vortex beam irradiates the Au film surface from the left side. The electron temperature at 15 fs (a), 1015 fs (b), 3 ps (c), and 11.4 ps (d); the phonon temperature at 15 fs (e), 1015 fs (f), 3 ps (g), and 11.4 ps (h). The topological charge of the vortex beam is taken as 1, the laser wavelength is 800 nm, the pulse duration is 30 fs, the two-pulse separation is 1 ps, and the respective sub-pulse fluence $F_1 = F_2 = 0.3$ J cm^{-2}. The surface width and the thickness of the 2D geometry are 6 μm and 1 μm, respectively. Here, the thickness is amplified by 3.75 times for good characterization of the ripple profile.

3. Results and discussion

The 2D maps of temperature modulation in the sub-layer ripple region of Au film induced by a femtosecond laser two-pulse vortex beam are shown in figure 1. It can be seen that the electron temperature field typically takes on a vortical profile loaded by the periodic ripples at 15 fs, a time accounting for the arrival of the first pulse peak of the vortex beam (figure 1(a)). As the second pulse of the vortex beam strikes the Au film surface, the electron temperature field modulation is violently re-amplified in the ripple region, producing a sharper profile at 1.015 ps (figure 1(b)). Following two-pulse irradiation, the temperature modulation for the electron system becomes increasingly blurred, which can be especially observed at 3 ps (figure 1(c)). This originates from the thermal degeneration in the electron system due to the aggressive dynamics of the electron thermal diffusion and the e–p coupling on the picosecond timescale. With time, the thermally degenerated ripple tends to stop its evolution at the termination of e–p coupling at 11.4 ps (figure 1(d)).

On the other hand, the temperature field for the phonon system remains less disturbed at the arrival of the first pulse peak of the vortex beam (figure 1(e)). Upon the arrival of the second vortex beam pulse peak at 1015 fs, an initial ripple phonon temperature profile is established within the sub-layer region of the Au film, as depicted in figure 1(f). The ripple phonon temperature profile becomes increasingly observable at 3 ps (figure 1(g)) due to the dominant e–p coupling dynamics that transfer the electron energy into the phonon system. At 11.4 ps, a sharp ripple profile in the phonon
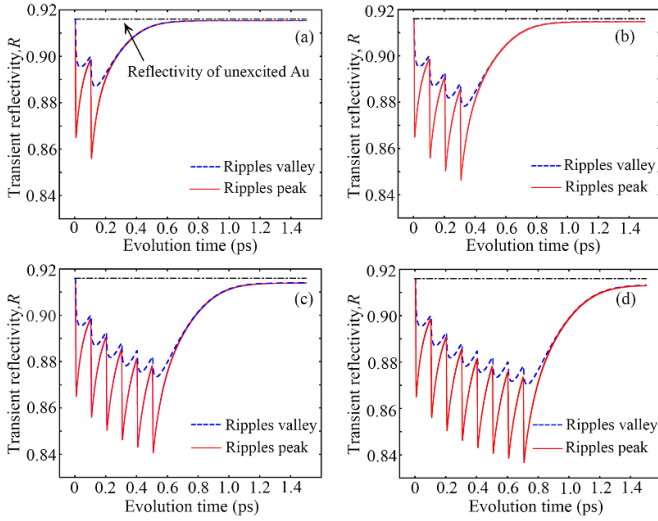
Figure 2. The transient reflectivity at ripple peaks and neighbouring valleys at the bright edge of the vortex beam with varying pulse numbers: (a) $N = 2$, (b) $N = 4$, (c) $N = 6$, (d) $N = 8$. The laser wavelength is centered at 800 nm, the pulse duration is 30 fs, the pulse separation is 1 ps and the respective sub-pulse fluence is set as 0.05 J cm^{-2}. The topological charge of the vortex beam is taken as 1.


Figure 3. The temporal temperature profiles for electrons and phonons at the peaks and valleys of ripples on an Au film induced by a femtosecond laser multi-pulse vortex beam: (a) electron system; (b) phonon system. The laser wavelength is centered at 800 nm, the pulse duration is 30 fs with a pulse separation of 1 ps. The respective sub-pulse fluence is set as 0.1 J cm^{-2}. The topological charge of the vortex beam is taken as 1.

temperature modulation region can significantly emerge at the termination of the e–p period (figure 1(h)). It should be noted that Fourier thermal diffusion will dominate the evolution of ripple temperature after the e–p dynamics, which is outside the current topic of ultrafast ripple dynamics and not considered here.

The transient reflectivities extracted at ripple peak and neighbouring valley positions on an Au film surface at the bright edge of a femtosecond laser vortex beam with varying pulse numbers are shown in figure 2. We see from figure 2(a) that the transient reflectivity abruptly drops from the unexcited state to values of 0.865 and 0.856 at the respective two pulse peaks for the basic configuration of two-pulse irradiation. The drop in reflectivity is more pronounced at the peak of ripples compared with the neighbouring valley at the bright edge of the vortex beam. The observed phenomenon can be attributed to the complex interplay of the dynamics of the temperature-dependent reflectivity in the ripple region under multi-pulse shots. It can be seen that the transient reflectivity exhibits multi-valley profiles following the multi-pulse shots (figures 2(b)–(d)). In particular, the depth of these reflectivity valleys increases with the number of pulses in the femtosecond laser vortex beam. Finally, the reflectivity trends to recover to the primitive level for unexcited Au on a picosecond timescale. The reflectivity recovery cycle, which is defined as the period for the reflectivity to recover, is typically increased by increasing the pulse number from two to four then six to eight. The reflectivity recovery cycle coincidentally falls into the e–p coupling period. Considering the fact that the e–p coupling process can be significantly prolonged for larger pulse numbers, the reflectivity recovery cycle is consequently expanded by increasing the pulse number of the femtosecond laser
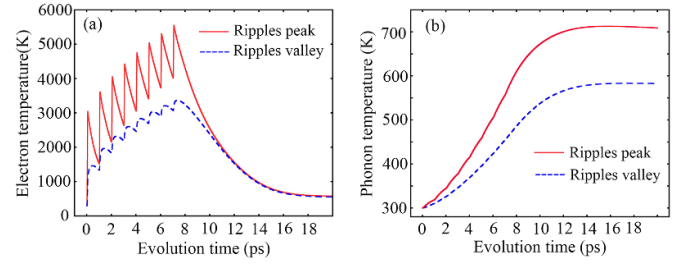
vortex beam. The results can provide the base for initially controlling the reflectivity, and thus the subsequent thermal dynamics during ripple modulation on the Au film.

The temporal temperature profiles for electrons and phonons at the peaks and valleys of ripples on an Au film induced by a femtosecond laser multi-pulse vortex beam are shown in figure 3. To fundamentally understand the dynamics of multi-pulse shots, an eight-pulse femtosecond laser vortex beam is employed in this study. It can be seen that sharp multi-peak profiles emerge at the peak position of the ripples (figure 3(a)). The peak electron temperature increases significantly as the number of pulses in the vortex beam increases from one to eight, with an evolution time in picoseconds. After all the pulse shots, the electron temperature profile experiences a continuous drop, finally becoming saturated. On the other hand, the phonon temperature at the peak and neighbouring valley of ripples exhibit a continuous rise with evolution time until saturation of the phonon temperature is reached at 14 ps.

In fact, thermal equilibrium occurs in the electron and phonon systems at 14 ps, giving rise to saturation of the phonon temperature of ripples. Importantly, the phonon temperature difference between the surface peak and the adjacent ripple valley becomes increasingly pronounced as the system approaches e–p coupling termination. This indicates that as thermal evolution approaches thermal equilibrium, sharp ripples tend to emerge due to the increasingly different phonon temperatures at the peaks and valleys of the ripples.

To explore the sharp appearance of the ripples, we define the ripple modulation contrast in terms of the phonon temperature, written as $C = (T_{peak} - T_{valley})/(T_{peak} + T_{valley})$. Here, T_{peak} and T_{valley} represent the available maximum phonon temperature at ripple peak and neighbouring valley positions at the termination of the e–p coupling period. As shown in figure 4(a), the ripple contrast exhibits a slight decrease from 12.5% to 11% when the pulse duration is increased from 30 fs to ~1.0 ps for two-pulse vortex beam irradiation. The ripple contrast tends to have an obvious rise from 1% to 15.2% with increasing sub-pulse fluence of the two-pulse vortex beam from 0.05 J cm^{-2} to 0.35 J cm^{-2} (figure 4(b)). The maximum phonon temperature also exhibits a similar tendency
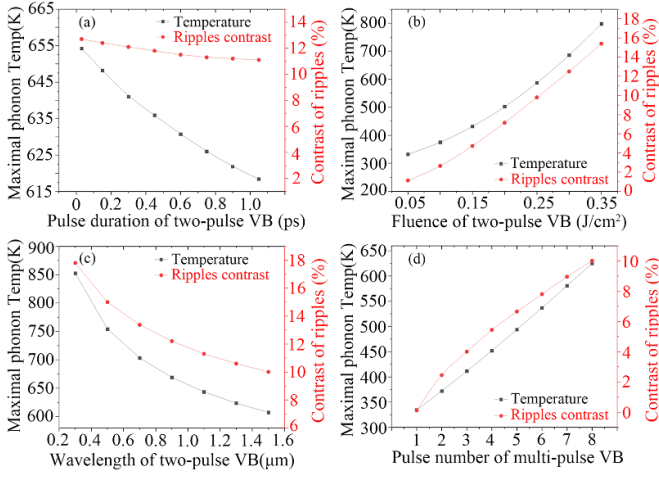
Figure 4. The maximum phonon temperature and the ripple contrast as a function of femtosecond laser vortex beam (VB) parameters. (a) The laser is centered at a wavelength of 800 nm, the two-pulse separation is 1 ps and the respective sub-pulse fluence is 0.3 J cm^{-2}. (b) The wavelength is centered at 800 nm, the pulse duration is 30 fs and the two-pulse separation is 1 ps. (c) The pulse duration is 30 fs, the two-pulse separation is 1 ps and the respective sub-pulse fluence is 0.3 J cm^{-2}. (d) The respective sub-pulse fluence is 0.1 J cm^{-2}, the laser wavelength is centered at 800 nm, the pulse duration is 30 fs and the pulse separation is 1 ps. The topological charge of the vortex beam is taken as 1.

with increasing vortex beam fluence. This indicates that a high laser fluence can achieve sharper ripples with high contrast due to the higher phonon temperature contrast. It can be seen from figure 4(c) that the ripple contrast shows a continuous drop from 17.9% to 10% with increasing laser wavelength from 300 nm to 1500 nm (figure 4(c)). The maximum phonon temperature also decreases from 850 K to 608 K, which is especially obvious in the ultraviolet and visible spectra rather than the infrared spectrum. The ripple contrast shows an obvious rise from 0.1% to 10% as the pulse number in the vortex beam increases from one to eight (figure 4(d)). Simultaneously, the maximum phonon temperature climbs from 327 K to 625 K with an increase in the number of pulses in the vortex beam up to eight pulses. It should be emphasized that the results are particularly right for the e–p non-equilibrium period during Au film excitation. In addition, the phonon temperature modulation will possibly be recorded as the maximum phonon temperature in the ripple region exceeds the phase explosion threshold, potentially forming patterned ripples. In this case, a more complex thermal-fluidics mechanism outside the non-equilibrium state needs to be considered in detail, and this is not the focus of the current investigation into low-thermal driven ripple formation in highly non-equilibrium Au film.

Understanding the ripple formation lifetime in the highly non-equilibrium state in the target material is fundamental for exploring the complex ripple dynamics. For this purpose, we explore the e–p coupling time as a function of the laser parameters of the femtosecond vortex beam as shown in figure 5. In the case of basic two-pulse irradiation, we can see that by increasing the pulse duration in the sub-picosecond time regime, the e–p coupling time exhibits a near-linear monotonic
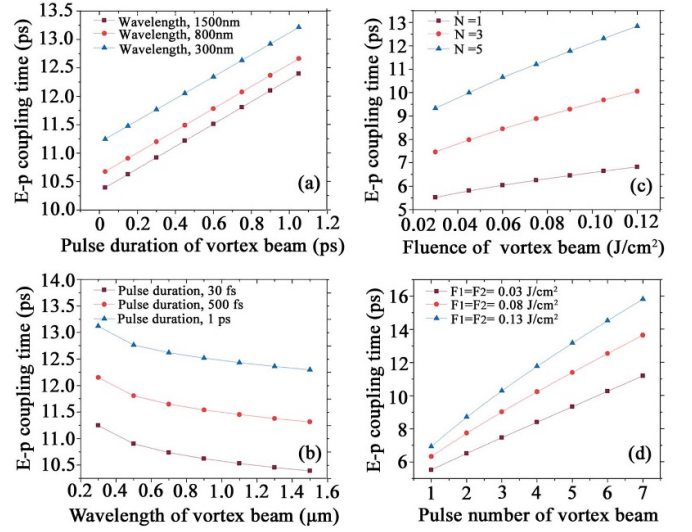
Figure 5. The electron–phonon (E–p) coupling time versus parameters of the femtosecond laser vortex beam. (a) Basic two-pulse irradiation: the pulse separation is 1 ps, and the respective sub-pulse fluence is 0.3 J cm^{-2}. (b) Basic two-pulse irradiation: the respective sub-pulse fluence is 0.3 J cm^{-2}, and the two-pulse separation is 1 ps. (c) A comparison of single-pulse ($N = 1$), three-pulse ($N = 3$), and five-pulse ($N = 5$) irradiations: the laser wavelength is centered at 800 nm, the pulse duration is 30 fs and the pulse separation is 1 ps. (d) Multi-pulse irradiations: the laser wavelength is centered at 800 nm, the pulse duration is 30 fs and the pulse separation is 1 ps. The topological charge of the vortex beam is taken as 1.

rise for the given wavelengths of 300 nm, 800 nm, and 1500 nm (figure 5(a)). As shown in figure 5(b), the e–p coupling time decreases continuously with increasing laser wavelength of the double-pulse vortex beam and eventually becomes saturated at specific values at pulse durations of 30 fs, 500 fs, and 1 ps, respectively. In addition, for one, three, and five pulses, we can see that the e–p coupling time increases by increasing the sub-pulse fluence of the vortex beam from 0.03 J cm^{-2} to 0.12 J cm^{-2} (figure 5(c)). In particular, the e–p coupling time increases faster for five pulses ($N = 5$), and three pulses ($N = 3$) rather than a single pulse ($N = 1$). The e–p coupling time shows an obvious rise with an increasing number of pulses in the vortex beam from one to seven for the given sub-pulse fluence of 0.03 J cm^{-2}, 0.08 J cm^{-2} and 0.13 J cm^{-2} (figure 5(d)). The results indicate that the dynamic lifetime of ripple formation can be desirably manipulated by elaborately designing the laser parameters of the femtosecond laser multi-pulse vortex beam. This study provides the basic route for parametrically controlling the e–p coupling dynamics by manipulating the femtosecond laser multi-pulse vortex beam.

In fact, the critical length of the diffusion of electrons can obey the law $L_c \sim \tau_R^{1/2}$, where τ_R is the e–p coupling time [35]. This provides a good opportunity to manipulate the thermal diffusion in a target by controlling the e–p coupling time. Our work has revealed that the e–p coupling time can be manipulated by varying the full parameters of the femtosecond laser multi-pulse vortex beam. This indicates that the electron thermal diffusion length can be substantially confined to a

J. Phys. D: Appl. Phys. **58** (2025) 045107

G Du *et al*

more localized space by controlling multiple parameters of the vortex beam, potentially beneficial for preparing high-quality ripples.

4. Conclusions

We have theoretically investigated the particular dynamics of thermal modulation during early ripple formation on an Au film upon irradiation with a femtosecond laser multi-pulse vortex beam. It is proposed that the transient reflectivity exhibits multi-valley profiles as a result of the multi-pulse shots. In particular, the ripple contrast tends to rise with increasing pulse number, or alternatively with enlarging the laser fluence of the vortex beam. On the contrary, the ripple contrast is obviously decreased by increasing the wavelength from ultraviolet to visible. The ripple contrast is less influenced by the pulse duration in the sub-picosecond regime. The electron–phonon coupling time during ripple formation shows a continuous increase in the picosecond time regime with increasing pulse duration, laser fluence, and pulse number of the vortex beam. The electron–phonon coupling time decreases with increasing laser wavelength and eventually tends to saturation. Our results could be helpful for understanding the basic dynamics of early ripple formation, advancing the cutting-edge applications of laser nanofabrication for ripple-biomimetic architecture, solar cells, and friction devices, etc.

Data availability statement

All data that support the findings of this study are included within the article (and any supplementary files).

ORCID iDs

Guangqing Du https://orcid.org/0009-0002-9307-342X
Waqas Ahmad https://orcid.org/0009-0003-4210-0253
Feng Chen https://orcid.org/0000-0002-7031-7404

References

[1] Luo X, Yao S L, Zhang H J, Cai M Y, Liu W J, Pan R, Chen C H, Wang X M, Wang L N and Zhong M L 2020 *Opt. Laser Technol.* **124** 105973
[2] Martínez-Calderon M, Martín-Palma R J, Rodríguez A, Gómez-Aranzadi M, García-Ruiz J P, Olaizola S M and Manso-Silván M 2020 *Phys. Rev. Mater.* **4** 056008
[3] Badía-Majós A, Martínez E, Angurel L A, de la Fuente G F, Fourneau E, Marinković S and Silhanek A V 2024 *Appl. Surf. Sci.* **649** 159164
[4] Zhang D S, Ranjan B, Tanaka T and Sugioka K 2020 *ACS Appl. Nano Mater.* **3** 1855–71
[5] Cihan E, Heier J, Lubig K, Gräf S, Müller F A and Gnecco E 2023 *ACS Appl. Mater. Interfaces* **15** 14970–8
[6] Kunz C, Bonse J, Spaltmann D, Neumann C, Turchanin A, Bartolomé J F, Müller F A and Gräf S 2020 *Appl. Surf. Sci.* **499** 143917
[7] Colombier J-P *et al* 2020 *Phys. Rev. Res.* **2** 043080
[8] Lu M, Cheng K, Qin Z Y, Ju J Q, Liu J K and Huo Y Y 2022 *Opt. Express* **30** 6
[9] Fraggelakis F, Tsibidis G D and Stratakis E 2021 *Phys. Rev.* B **103** 054105
[10] Terekhin P N, Benhayoun O, Weber S T, Ivanov D S, Garcia M E and Rethfeld B 2020 *Appl. Surf. Sci.* **512** 144420
[11] Lingos P, Perrakis G, Tsilipakos O, Tsibidis G D and Stratakis E 2023 *Opt. Laser Technol.* **163** 109415
[12] Tsibidis G D, Lingos P and Stratakis E 2022 *Opt. Lett.* **47** 4251
[13] Zuhlke C A, Tsibidis G D, Anderson T, Stratakis E, Gogos G and Alexander D R 2018 *AIP Adv.* **8** 015212
[14] Wang J C and Guo C L 2005 *Appl. Phys. Lett.* **87** 251914
[15] Garrelie F, Colombier J P, Pigeon F, Tonchev S, Faure N, Bounhalli M, Reynaud S and Parriaux O 2011 *Opt. Express* **19** 10
[16] Tsibidis G D, Barberoglou M, Loukakos P A, Stratakis E and Fotakis C 2012 *Phys. Rev.* B **86** 115316
[17] Fuentes-Edfuf Y, Sánchez-Gil J A, Florian C, Giannini V, Solis J and Siegel J 2019 *ACS Omega* **4** 6939–46
[18] Apostolova T, Obreshkov B D, Ionin A A, Kudryashov S I, Makarov S V, Mel'nik N N and Rudenko A A 2018 *Appl. Surf. Sci.* **427** 334–43
[19] Skoulas E, Tasolamprou A C, Kenanakis G and Stratakis E 2020 *Appl. Surf. Sci.* **541** 148470
[20] Nivas J J J, Cardano F, Song Z M, Rubano A, Fittipaldi R, Vecchione A, Paparo D, Marrucci L, Bruzzese R and Amoruso S 2017 *Sci. Rep.* **7** 42142
[21] Romashevskiy S A, Ashitkov S I and Agranat M B 2020 *Opt. Lett.* **45** 4
[22] Tang Y, Perrie W, Sierra D R, Li Q L, Liu D, Edwardson S P and Dearden G 2021 *Micromachines* **12** 376
[23] Kawaguchi H, Yasuhara R, Yang H T, Hori C, Miyagawa R, Sugioka K, Ota M and Uehara H 2024 *Opt. Mater. Express* **14** 21
[24] Nivas J J J, He S T, Song Z M, Rubano A, Vecchione A, Paparo D, Marrucci L, Bruzzese R and Amoruso S 2017 *Appl. Surf. Sci.* **418** 565–71
[25] Du G Q, Yu F R, Lu Y, Kai L, Yang Q, Hou X and Chen F 2023 *Int. J. Therm. Sci.* **187** 108208
[26] Du G Q, Yu F R, Waqas A and Chen F 2024 *Opt. Laser Technol.* **174** 110619
[27] Ritzmann U, Oppeneer P M and Maldonado P 2020 *Phys. Rev.* B **102** 214305
[28] Taylor L L, Scott R E and Qiao J 2018 *Opt. Mater. Express* **8** 3
[29] Tsibidis G D, Mouchliadis L, Pedio M and Stratakis E 2020 *Phys. Rev.* B **101** 075207
[30] Hlinomaz K, Levy Y, Derrien T J-Y and Bulgakova N M 2022 *Int. J. Heat Mass Transfer* **196** 123292
[31] Du G Q, Yang Q, Chen F, Si J H and Hou X 2011 *Appl. Surf. Sci.* **257** 9177–82
[32] Anisinov S I, Kapeliovich B L and Perel'man T L 1974 *Sov. Phys.–JETP* **39** 375–7
[33] Chen J K, Tzou D Y and Beraun J E 2006 *Int. J. Heat Mass Transfer* **49** 307–16
[34] Chen A M, Xu H F, Jiang Y F, Sui L Z, Ding D J, Liu H and Jin M X 2010 *Appl. Surf. Sci.* **257** 1678–83
[35] Wellershoff S-S, Hohlfeld J, Güdde J and Matthias E 1999 *Appl. Phys.* A **69** S99–S107